RSC Sustainability

ROYAL SOCIETY OF CHEMISTRY

PAPER

View Article Online
View Journal

Cite this: DOI: 10.1039/d6su00210b

Ambient, two-step CO_2-to-$CaCO_3$ conversion: alkali-activated H_2O_2-promoted carbonate CO_2 capture and direct calcite mineralization

Eugene Shirman * and Yoel Sasson

Received 11th April 2026
Accepted 9th May 2026

DOI: 10.1039/d6su00210b

rsc.li/rscsus

We demonstrate an ambient-temperature two-step CO_2-to-$CaCO_3$ conversion in which alkali-activated H_2O_2 accelerates carbonate CO_2 capture, followed by calcite mineralization upon $CaCl_2$ addition, without thermal stripping of the capture liquor. Alkali activation generates transient reactive oxygen species (ROS) that promote rapid CO_2 absorption at 30 °C into aqueous Na_2CO_3 and K_2CO_3 without persistent promoters, yielding bicarbonate-rich liquors that are directly mineralized to phase-pure calcite and release a CO_2 stream free of O_2. Single-reactor screening identified concentration windows that maximize capacity while maintaining homogeneity, with Na_2CO_3 optimal near 7–10 wt% and K_2CO_3 near 20–25 wt%. Multi-reactor staging prolonged cycle duration and moderated the trade-off between outlet CO_2-removal specification and first-stage carbonate-to-bicarbonate conversion, with K_2CO_3 formulations showing the smallest penalty at stricter cutoffs. The $CaCO_3$ products were identified as calcite by XRD and ATR-FTIR, with SEM/EDS results consistent with rhombohedral $CaCO_3$ and no detectable secondary elements. A consumables-only techno-economic analysis using four geography-specific reagent price decks shows that LCOC is reagent-dominated, with carbonate utilization emerging as the principal cost lever through its effect on stoichiometric make-up demand. Overall, the results establish an ambient-temperature capture-to-mineralization route in which alkali-activated H_2O_2-derived ROS accelerate carbonate capture and direct mineralization avoids thermal regeneration.

Sustainability spotlight

Decarbonizing point-source CO_2 capture demands low-energy routes that avoid amine regeneration and degradation. We demonstrate an ambient-temperature capture-to-conversion scheme in which alkali-activated, H_2O_2-derived ROS transiently promote carbonate CO_2 absorption at 30 °C and then self-dissipate, yielding bicarbonate liquors free from persistent promoter residues that precipitate phase-pure calcite with $CaCl_2$; multi-reactor staging maintains high removal while preserving carbonate utilization. The chemistry uses commodity inputs (Na_2CO_3/K_2CO_3, H_2O_2, $CaCl_2$), eliminates thermal stripping, and yields a utilizable $CaCO_3$ product and an O_2-free CO_2 stream, highlighting a simple path to lower thermal energy demand and clearer pathways for future cost reduction through improved utilization, regeneration, and waste-derived reagents. This advance supports SDG 13 (Climate Action), SDG 9 (Industry, Innovation and Infrastructure), and SDG 12 (Responsible Consumption and Production).

1 Introduction

The increasing atmospheric concentration of CO_2 is a major driver of global climate change, requiring action to reduce emissions and achieve net-zero targets by mid-century.[1–3] Carbon capture, utilization, and storage (CCUS) technologies are widely regarded as a central pillar of decarbonization, enabling substantial reductions in emissions from point sources and, potentially, from the atmosphere itself.[4,5] Within the portfolio of existing CO_2 capture methods, amine-based absorption, particularly with monoethanolamine (MEA), is the most mature and widely applied industrial method.[6–8] However, amine-based absorption systems suffer from well-documented disadvantages, including high energy requirements for thermal regeneration (typically 3.6–4.0 GJ t^{-1} CO_2), as well as thermal and oxidative degradation, corrosivity, volatility, and aerosol emissions.[4,9] These challenges impose both economic and environmental costs, limiting large-scale deployment.[4,10] Consequently, there is considerable interest in developing CO_2 capture strategies that reduce energy penalties, minimize environmental impacts, and enable direct integration with carbon utilization pathways to produce valuable products.[11,12]

Alkaline carbonate solutions, such as potassium carbonate (K_2CO_3) and sodium carbonate (Na_2CO_3), are promising alternatives to amines due to their low cost, low volatility, negligible toxicity, and high chemical stability.[13–15] K_2CO_3-based processes, such as the Benfield process (also known as the hot

Casali Center of Applied Chemistry, Institute of Chemistry, The Hebrew University of Jerusalem, Jerusalem, 9190401, Israel. E-mail: eugene.shirman@mail.huji.ac.il

potassium carbonate process), have already been implemented for CO_2 and H_2S removal in more than 600 plants, demonstrating their industrial maturity.[16,17] Furthermore, carbonate-based systems have lower regeneration energy requirements than amines and avoid the degradation products associated with the latter.[14,18] Nevertheless, their main limitation is the relatively slow CO_2 absorption kinetics, particularly under ambient conditions.[14,19] Industrial processes such as the hot potassium carbonate process address this limitation by operating at elevated absorption temperatures (~100–120 °C) and employing rate promoters, such as piperazine and amino acids, to accelerate the bicarbonate formation step.[20–22] These promoters are commonly classified into three groups: organic, inorganic, and enzymatic.[14,23] While effective for CCS, the persistence of organic promoters (such as amines or amino acids) leaves chemical residues in the resulting bicarbonate liquor. Integrating these promoted solutions directly into CCU processes can therefore complicate downstream conversion or necessitate additional separation steps to recover the capture agents.[24–26]

Recently, we presented a novel kinetic promotion method for K_2CO_3 solutions that utilizes hydrogen peroxide (H_2O_2)-derived reactive oxygen species (ROS) as promoters for CO_2 absorption by K_2CO_3.[26] Mechanistically, we treat ROS as transient, *in situ* promoters that accelerate the otherwise slow bicarbonate-forming chemistry in carbonate capture under near-ambient conditions, while decomposing to benign products and therefore not persisting into downstream mineralization. This approach achieved CO_2 uptake rates at room temperature comparable to those of piperazine-promoted systems, while leaving a promoter-free bicarbonate-rich solution after ROS decomposition. In strongly alkaline media, where H_2O_2 is partially deprotonated as HO_2^- ($pK_a \approx 11.6$ at 25–30 °C), small additions of H_2O_2 generate transient ROS under ambient conditions, including superoxide ($O_2^{\bullet-}$), hydroxyl radicals ($^{\bullet}OH$), and singlet oxygen ($^1O_2$).[27–30]

$$H_2O_2 + OH^- \rightleftharpoons HO_2^- + H_2O \quad (1)$$

In related systems, oxygen-centered radical species have been reported to react rapidly with CO_2 to give transient oxygenated intermediates; such chemistry offers a plausible kinetic basis for enhanced bicarbonate formation under strongly basic conditions.

$$X_2CO_3 + CO_2 + H_2O \rightleftharpoons 2XHCO_3 \text{ (X = Na or K; promoted by transient ROS)} \quad (2)$$

For clarity, eqn (1) and (2) summarize the chemistry at the process level: alkaline peroxide activation generates transient promoter species, and the overall promoted capture step converts carbonate to bicarbonate; however, the present study does not seek to distinguish among the possible underlying elementary ROS-mediated pathways.

Our previous work demonstrated that ROS, including superoxide, can facilitate the carbonate-to-bicarbonate conversion.[26] Earlier work by our group demonstrated *in situ* superoxide generation upon introducing H_2O_2 to NaOH and KOH solutions.[31,32] In this study, our approach omits the addition of excess caustic, relying instead on the hydroxide inherently present at the alkaline pH of K_2CO_3 (or Na_2CO_3) solutions to enable peroxide activation. The self-dissipating nature of ROS offers a unique advantage: the resulting bicarbonate-rich liquor can be directly repurposed for downstream utilization without additional purification. Economically, commodity H_2O_2 can be competitive with organic promoters and avoids amine-derived degradation products. To circumvent the substantial energy penalty associated with conventional CCUS technologies, carbonate mineralization has been explored as a low-energy chemical conversion route.[33,34] Within the literature, carbonate mineralization approaches are broadly divided into direct gas–solid mineralization at elevated temperatures and pressures, and indirect aqueous mineralization at ambient conditions.[13,34] For positioning the present work within the broader aqueous alkaline CO_2-capture literature, two process archetypes are especially relevant: (i) chemical regeneration (looping) approaches, in which the alkaline capture capacity is restored while $CaCO_3$ precipitates (*e.g.*, causticization/looping schemes);[35,36] and (ii) single-pass capture-and-conversion routes. In the latter, the bicarbonate liquor is consumed stoichiometrically to form $CaCO_3$ (and a corresponding brine), a step that can be coupled with the release of a concentrated CO_2 stream without thermal stripping.[13]

Barzagli *et al.* reported a similar two-step process in which CO_2 is first absorbed into an aqueous Na_2CO_3 solution, and the resulting bicarbonate-rich liquor is then reacted with $CaCl_2$ at room temperature to yield $CaCO_3$ and high-purity CO_2.[13] This method eliminates the need for thermal stripping by chemically transforming $NaHCO_3$ into $CaCO_3$. However, its reliance on dilute Na_2CO_3 solutions, limited CO_2 removal thresholds (~80%), and the intrinsically slow kinetics of unpromoted carbonate absorption present challenges for scale-up. Improving the kinetics and enabling the use of more concentrated solutions could enhance the practicality of such ambient-temperature capture-conversion schemes.

In this work, we present an improved two-step CO_2 capture and utilization process that combines ROS-promoted carbonate absorption with subsequent $CaCO_3$ precipitation. In the first step, CO_2 is absorbed into aqueous alkali carbonate solution containing a small concentration of H_2O_2 (typically one-tenth of the carbonate concentration), enabling rapid CO_2 uptake at 30 °C and high bicarbonate conversion while preventing precipitation. A transient O_2 signal occurs only in promoted runs during CO_2 absorption, typically peaking early but not confined to the onset, and is used solely as a diagnostic of promoter activity.

The promotion is self-terminating as CO_2 loading reduces alkalinity toward the HO_2^-/H_2O_2 boundary, yielding a bicarbonate-rich liquor without persistent promoter residues. Both K_2CO_3 and Na_2CO_3 were investigated to assess how carbonate solubility and cation identity influence ROS-promoted uptake and downstream precipitation, and to quantify the associated cost-performance trade-offs. In the second step, the bicarbonate-rich solution, free from persistent promoters, is

treated with $CaCl_2$ to precipitate pure calcite $CaCO_3$ and release CO_2, as summarized in eqn (3).

$$2XHCO_3 + CaCl_2 \rightarrow CaCO_3\downarrow + 2XCl + CO_2 + H_2O\ (X = Na\ or\ K) \quad (3)$$

This single-pass design simplifies operation, avoids thermal regeneration, and yields phase-pure calcite and a CO_2 stream with O_2 below the detection limit. In our bench configuration this gas is N_2-balanced due to the inert sweep; the headspace composition thus reflects the sweep rather than the chemistry. To sustain CO_2-removal efficiency setpoints of 80%, 90%, and 100%, cycles were terminated at the corresponding CO_2 outlet threshold. Through single- and multi-reactor configurations, we evaluate the kinetics, bicarbonate conversion, and product quality, demonstrating the potential of this approach as a sustainable, low-energy CCU pathway.

2 Experimental

2.1 CO_2 absorption and conversion setup

Single-reactor CO_2 absorption experiments were conducted using the system described in our previous work.[27] A stirred reactor containing an aqueous carbonate/H_2O_2 solution was supplied with a CO_2/N_2 gas mixture (15 vol% CO_2 in N_2) at a constant flow rate of 0.2 L min^{-1}, controlled by a mass flow controller (Aalborg DPC 17). The gas was introduced through a sintered glass diffuser to ensure efficient dispersion. The reactor was immersed in a thermostated bath at 30 ± 1 °C.

Outlet CO_2 and O_2 concentrations were logged every 20 s using an NDIR CO_2 sensor (Senseair K33 BLG) and a fluorescence-based O_2 sensor (LuminOx UV Flux). The first 2 min of recorded data correspond to an effective deadtime arising from gas transport lag in the sampling line. Baseline tests at 15 vol% CO_2/N_2 gave standard deviations of ±0.047–0.158 vol% after deadtime, well below the manufacturer accuracy (±0.5 vol% + 3% of reading). Instrument specifications are therefore taken as error bounds. The CO_2 removal efficiency (E) was calculated according to eqn (4):

$$E = \frac{C_i - C_o}{C_i} \times 100 \quad (4)$$

where C_i and C_o denote the inlet and outlet CO_2 concentrations, respectively.

To provide non-ambient controls, we performed a single-reactor temperature series (25, 30, 50, and 70 °C; ±1 °C) for 30 wt% K_2CO_3 + 3 wt% H_2O_2 (15 g) under the same feed conditions as above (15 vol% CO_2/N_2, 0.2 L min^{-1}). CO_2 capacity (mmol CO_2 per g solution) was obtained by integrating the inlet-outlet CO_2 difference ($C_i - C_o$), over time.

For multi-reactor tests, two or three identical reactors were connected in series. The feed gas flow rate was adjusted to 0.35 L min^{-1} (two reactors) or 0.5 L min^{-1} (three reactors). The lead reactor was maintained at 30 ± 1 °C, while downstream reactors were operated at room temperature. Runs were continued until the train-averaged CO_2 removal efficiency fell below predefined thresholds (80%, 90%, or 100%). Each condition was tested over three consecutive cycles. Between cycles, the lead reactor was removed for $CaCl_2$ treatment, the train was advanced by one position, and the tail stage was replenished with fresh absorbent.

The CO_2 absorption-conversion configuration is illustrated in Fig. 1, which schematically shows the staged multi-reactor absorption setup (Step 1) and the subsequent $CaCO_3$ precipitation stage (Step 2). In Step 2, the bicarbonate-rich solution was reacted with a stoichiometric $CaCl_2$ solution at ambient temperature, while N_2 was supplied at 0.2 L min^{-1}. This process yielded solid $CaCO_3$, an O_2-free CO_2 stream carried by the N_2 sweep, and a brine (NaCl or KCl, depending on the starting carbonate). The $CaCO_3$ precipitate was collected by filtration, washed with deionized water, and dried at 60 °C prior to characterization.

For representative multi-reactor runs, pH was measured to track alkalinity changes during CO_2 loading and subsequent

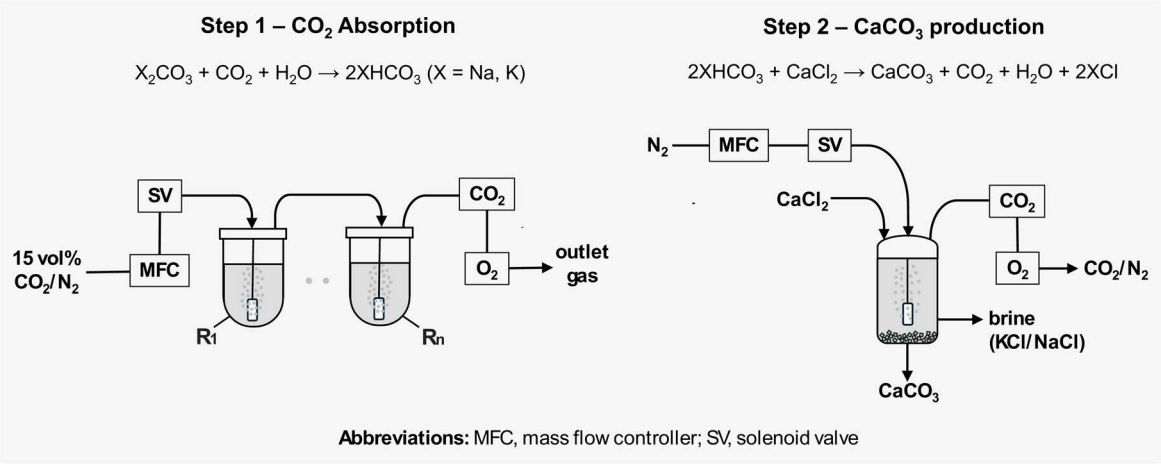

Fig. 1 Schematic representation of the experimental two-step CO_2 capture-to-$CaCO_3$ process. In the absorption step, a 15 vol% CO_2/N_2 stream is delivered *via* a mass flow controller and solenoid valve to stirred reactors connected in series, generating a bicarbonate-rich solution. R_1 denotes the first reactor in the series, whereas R_n denotes the final reactor, with $n = 2$ or 3 depending on the number of reactors employed. In the $CaCO_3$ production step, the bicarbonate-rich solution is reacted with $CaCl_2$ under N_2 flow to yield $CaCO_3$ and the corresponding salt brine.

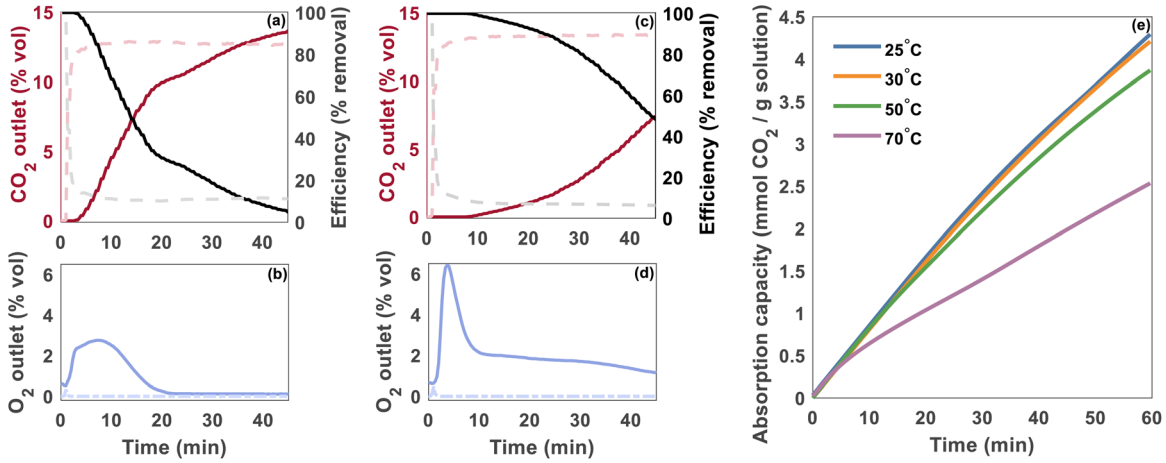

Fig. 2 Single-reactor CO_2 absorption behavior and temperature control experiments. Panels (a and b): 7 wt% Na_2CO_3 + 0.7 wt% H_2O_2; panels (c and d): 20 wt% K_2CO_3 + 2 wt% H_2O_2, each at 30 °C using 15 vol% CO_2/N_2 (0.2 L min^{-1}) and 15 g solution. (a and c) CO_2 outlet concentration (red) and removal efficiency (black); (b and d) O_2 outlet signal. Dashed curves represent the corresponding unpromoted solutions. (e) CO_2 absorption capacity *versus* time for 30 wt% K_2CO_3 + 3 wt% H_2O_2 at 25, 30, 50, and 70 °C (same gas feed and solution mass).

mineralization. Measurements were performed for 7 wt% Na_2CO_3 + 0.7 wt% H_2O_2 and 25 wt% K_2CO_3 + 2.5 wt% H_2O_2 at the 90% train-averaged CO_2-removal threshold. pH in reactor 1 was monitored at four stages: in the fresh starting solution before cycle 1, in the CO_2-loaded liquor at the end of cycle 1 immediately before $CaCl_2$ addition, in the corresponding liquor at the end of cycle 2, and in the recovered brine after $CaCO_3$ precipitation.

2.2 ^{13}C NMR analysis of carbonate/bicarbonate speciation

Post-absorption solution samples were analyzed by ^{13}C NMR spectroscopy using a Bruker Avance NEO 500 MHz spectrometer. Bicarbonate conversion was quantified from a linear regression of carbonate/bicarbonate chemical shifts (δ, ppm) against their molar fraction (χ), following an established method (R^2 = 0.9996, RMSE = 0.008).[26,37] The bicarbonate conversion was quantified with reference to the carbonate/bicarbonate equilibrium corresponding to eqn (2).

Analytical uncertainty was taken as the calibration residual (±0.8% conversion), since the propagated peak-fit error (<0.1%) was negligible. Error bars in Fig. 4 and 6 reflect this uncertainty.

2.3 Characterization of $CaCO_3$ precipitates

The solid $CaCO_3$ obtained after absorption-conversion cycles was characterized by X-ray diffraction (XRD, Bruker D8 Advance), scanning electron microscopy with energy-dispersive X-ray spectroscopy (SEM/EDS, Thermo Fisher Scientific Apreo 2), and attenuated total reflectance Fourier-transform infrared spectroscopy (ATR-FTIR, Shimadzu IRAffinity-1S).

3 Results and discussion

3.1 Single-reactor screening of carbonate/H_2O_2 systems

Screening experiments were first conducted in a single stirred reactor to obtain CO_2 uptake curves and capacity, track O_2 evolution as a promoter diagnostic, and establish precipitation limits at 30 °C. Fig. 2 depicts the CO_2 absorption performance of two representative solutions from this single-reactor screening: 7 wt% Na_2CO_3 + 0.7 wt% H_2O_2 and 20 wt% K_2CO_3 + 2 wt% H_2O_2, operated at a flow rate of 0.2 L min^{-1} of a 15 vol% CO_2/N_2 mixture, contacting 15 g of solution. Panels (a andc) show the outlet CO_2 concentration and the corresponding removal efficiency, and panels (b andd) show the simultaneously measured O_2. Dashed curves in panels (a–d) represent the corresponding unpromoted (neat) Na_2CO_3 and K_2CO_3 solutions of equivalent carbonate concentration, included for comparison. The promoted systems show distinctly higher CO_2 removal efficiency and measurable O_2 evolution, in clear contrast to the unpromoted baselines, which exhibit minimal O_2 and a rapid breakthrough. Both systems begin at ~100% removal (outlet CO_2 ≈ 0%). The Na-based liquor shows an early CO_2 breakthrough (≈3 min) and a modest, broad O_2 peak (≈2.5 vol%) that decays to a zero baseline within the first half of the run. The K-based liquor maintains quantitative removal for ~9 min, exhibits a taller and narrower O_2 burst (peak ≈ 6.5 vol%) coincident with that period, followed by a slowly decaying non-zero O_2 baseline while CO_2 removal efficiency declines gradually over the remainder of the 45 min run.

For Na_2CO_3, the profiles are readily divided into three regions: (i) an initial interval of quantitative capture with a rising O_2 signal, indicating abundant HO_2^-/ROS at very high alkalinity, (ii) a transition where both the O_2 level and the removal efficiency decline as CO_2 loading lowers alkalinity, and (iii) a bicarbonate-rich interval in which O_2 is at baseline, below the analyzer's detection limit, and the CO_2 removal efficiency declines to low levels. This behavior is consistent with the promoter being effectively "off" as the solution nears the HO_2^-/H_2O_2 acid–base boundary (pK_a ≈ 11.6 at 25–30 °C), where the HO_2^- fraction and the ROS-driven O_2 release become negligible.

For K_2CO_3, the mechanism is essentially the same, albeit persisting longer due to higher solubility and higher carbonate/H_2O_2 loadings, which sustain promoter activity in the homogeneous regime. The O_2 peak falls within the 100%-removal window and is followed by a slowly decaying O_2 baseline

Table 1 Screening space and phase behavior at 30 °C

System	Conc. (wt%)	Homogeneous during run at 30 °C (max time observed)	Precipitation during operation (first observed)	Cooling-induced precipitation after run
Na_2CO_3	5	60 min	None	None
Na_2CO_3	7	60 min	None	None
Na_2CO_3	10	55 min	None during ≤55 min	Appears after ≥35 min runs
Na_2CO_3	15	≤30 min	By ~30 min	Appears after ≥20 min runs
Na_2CO_3	20[a]	n/a	By ~20 min	n/a
Na_2CO_3	30[a]	n/a	<10 min	n/a
K_2CO_3	10	60 min	None	None
K_2CO_3	20	60 min	None	None
K_2CO_3	25	50 min	By 60 min	Appears after ≥50 min runs
K_2CO_3	30	40 min	By ~45 min	Appears after ≥40 min runs

[a] Outside Fig. 3 but observed in screening; included here for completeness.

starting at ~2 vol%, consistent with the slower decline in CO_2 removal efficiency.

To benchmark the 30 °C operating condition against lower and elevated temperatures, an additional single-reactor temperature series (25, 30, 50, and 70 °C) was performed for 30 wt% K_2CO_3 + 3 wt% H_2O_2, and the resulting CO_2 absorption capacity profiles (mmol CO_2 per g solution) *versus* time are shown in Fig. 2e. This formulation was selected as a high-loading, high-signal case to isolate temperature effects under otherwise identical conditions and is used here as a control comparison rather than as a proposed optimum composition. The 25 and 30 °C traces are similar, with 25 °C showing only a marginally higher capacity, whereas capacity decreases at 50 °C and declines further at 70 °C. This monotonic reduction with temperature is consistent with faster H_2O_2 decomposition and increased self-quenching of ROS at elevated temperature, which shortens the effective promotion window for carbonate-to-bicarbonate conversion. Temperatures below 25 °C were not pursued further because they increased the tendency toward premature precipitation and would require active cooling, introducing an additional energy penalty.

Table 1 summarizes the single-reactor screening, listing the concentration-time windows tested and the onset of precipitation during operation at 30 °C and upon post-run cooling to room temperature. The performance outcomes across the homogeneous window, reported in Table 1, informed the selection of multi-reactor conditions (Section 3.2).

Fig. 3 maps the specific CO_2 capacity (mmol CO_2 per g solution) *versus* run time (0–60 min) and concentration for (a) Na_2CO_3 (5–15 wt%) and (b) K_2CO_3 (10–30 wt%) at 30 °C, across the concentration-time windows summarized in Table 1. Na_2CO_3 loadings above 15 wt% (20–30 wt%) were excluded, as these solutions precipitated prematurely in operation or on cooling, which placed them outside the homogeneous operating window. Surfaces smoothed from discrete runs indicate apparent capacities of ~0.4–2.1 mmol g^{-1} for Na and ~0.5–3.8 mmol g^{-1} for K (from the color scales).

For Na_2CO_3, capacity rises steeply during the first 15–20 min across all concentrations, reaching ~1.0 mmol g^{-1}. At lower loadings (5–7 wt%), the increase slows thereafter and plateaus near ~1.4 mmol g^{-1} after ~30 min, reflecting the intrinsic limit of these dilute solutions. At higher loadings, capacity continues to grow with time, reaching a maximum near 10 wt% where it

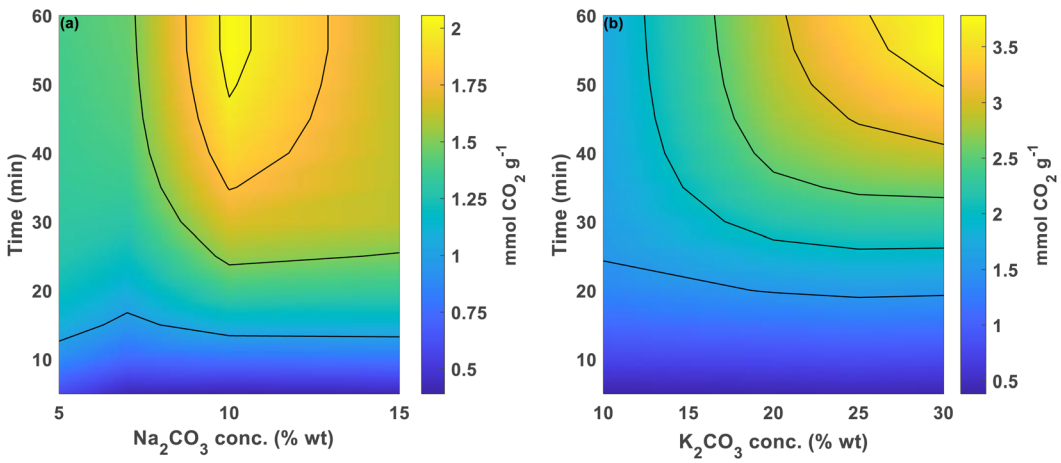

Fig. 3 Specific CO_2 capacity (mmol CO_2 per g solution) as a function of run time and carbonate concentration at 30 °C for (a) Na_2CO_3 (5–15 wt%) and (b) K_2CO_3 (10–30 wt%).

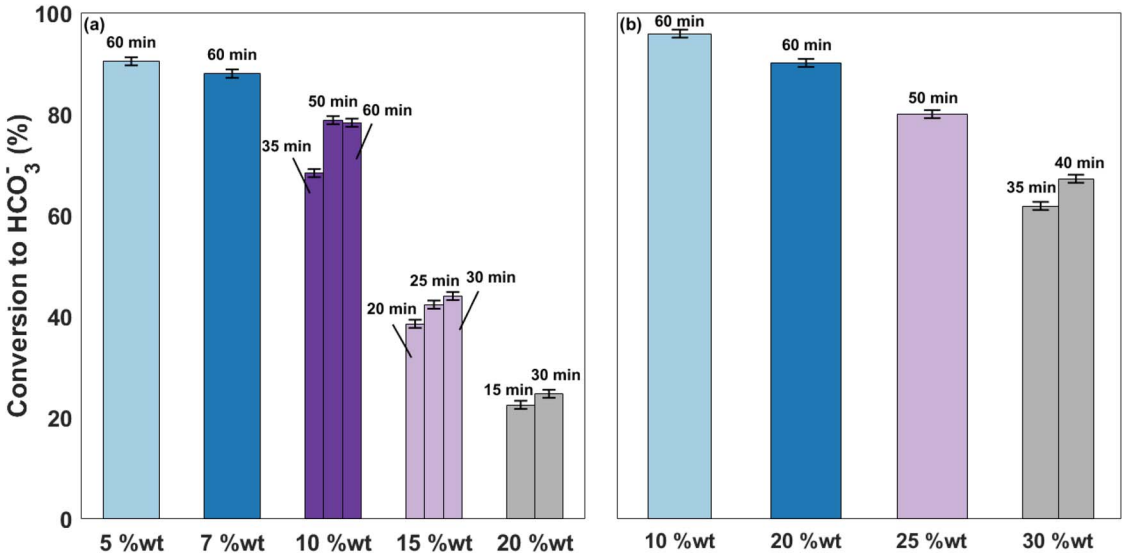

Fig. 4 Extent of carbonate-to-bicarbonate conversion (%) at 30 °C, determined by ^{13}C NMR of endpoint aliquots for single-reactor runs of (a) Na_2CO_3 solutions and (b) K_2CO_3 solutions. Run times (shown above bars) correspond to the endpoint aliquots used for NMR analysis. At higher carbonate loadings, these runs approach or exceed the precipitation limits summarized in Table 1.

peaks at ~2.1 mmol g^{-1} at 55–60 min. Beyond this mid-range, more concentrated solutions level off earlier due to precipitation, reinforcing 9–11 wt% as the region of highest attainable capacity. By contrast, K_2CO_3 increases more monotonically with concentration and time; at 30 wt% the run is truncated by in-run precipitation beginning at ~45 min, at which point the capacity is ~3.1–3.3 mmol g^{-1}. Thus, the observed ceiling at 30 wt% is set by time-to-solids, not by an intrinsic capacity limit. Within the homogeneous window, higher K_2CO_3 concentrations and longer times consistently deliver greater capacities.

Several compositions remain homogeneous at 30 °C but precipitate on cooling to room temperature (Na_2CO_3: 10–15 wt%; K_2CO_3: 25–30 wt%), distinguishing the in-run operating window from the post-run window and informing the process sequence. To avoid unintended solids, the absorber liquors should be kept at 30 °C through $CaCl_2$ addition, especially near the upper concentration/time edges, so that the only intentional precipitation is $CaCO_3$ during the second step of the 2-step process.

Fig. 4 links capacity to base utilization by reporting the extent of carbonate-to-bicarbonate conversion at the end of each single-reactor run at 30 °C, determined from ^{13}C NMR speciation of endpoint aliquots. Run times are shown above the bars. Panel (a) covers Na_2CO_3 (5–20 wt%) and panel (b) K_2CO_3 (10–30 wt%). For dilute-to-intermediate compositions, these runs fall within the homogeneous operating window, whereas the highest-loadings illustrate endpoint behavior near or beyond the precipitation boundary identified in Table 1.

For Na_2CO_3, the most dilute liquors (5 and 7 wt%) reach ~90% HCO_3^- after 60 min, indicating that nearly all of the initially charged carbonate is utilized. At 10 wt% the conversion is ~80% after a 50 min run, and it declines at higher loadings: 15 wt% levels off near 45% by 30 min, whereas 20 wt% reaches only ~25% over the same period. These results, together with the capacity maximum near 9–11 wt% in Fig. 3 and the earlier onset of in-run precipitation at higher Na_2CO_3 loadings, indicate that approximately 10 wt% Na_2CO_3 offers the best balance between attainable capacity and carbonate utilization.

Over comparable run durations, K_2CO_3 shows a markedly smaller fraction of residual carbonate. At 10 wt% the conversion is ≥95% at 60 min; at 20 wt% it is ~90% at 60 min. Even at 25 wt% conversion is ~80% by 50 min, whereas at 30 wt% it remains ~60–70% by 35–40 min. This pattern echoes the monotonic capacity rise and delayed precipitation mapped in Fig. 3 and Table 1.

Overall, the single-reactor screening results (Table 1, Fig. 3 and 4) define the operating windows used in the multi-reactor experiments discussed next. Na_2CO_3 should be maintained near 7–10 wt% to ensure both high base utilization and a homogeneous liquor at 30 °C, whereas K_2CO_3 can be increased to 20–25 wt% without significantly reducing conversion and carbonate residuals or triggering premature solids.

3.2 Multi-reactor operation of carbonate/H_2O_2 systems

We implemented cyclic absorption in two- and three-reactor trains to improve CO_2-removal efficiency while keeping the first reactor under the conditions established in the single-reactor screening. The aim of staging is not to increase total throughput, but to maintain high carbonate-to-bicarbonate conversion in the lead reactor while holding a tight outlet CO_2 specification throughout the run. Fig. 5 presents three successive cycles at 30 °C for four carbonate/H_2O_2 formulations: 7 wt% Na_2CO_3 + 0.7 wt% H_2O_2, 10 wt% Na_2CO_3 + 1 wt% H_2O_2, 20 wt% K_2CO_3 + 2 wt% H_2O_2, and 25 wt% K_2CO_3 + 2.5 wt% H_2O_2. Panels (a, c, e and g) show the train-averaged CO_2 removal efficiency for the three cycles, and panels (b, d, f and h) show the corresponding O_2 outlet traces for cycle 2, time-aligned with the CO_2 data. The 7 wt% Na and 20 wt% K cases ran as three-reactor trains at 0.5 L min; the 10 wt% Na and 25 wt% K cases ran as two-reactor trains at 0.35 L min^{-1} to avoid early precipitation

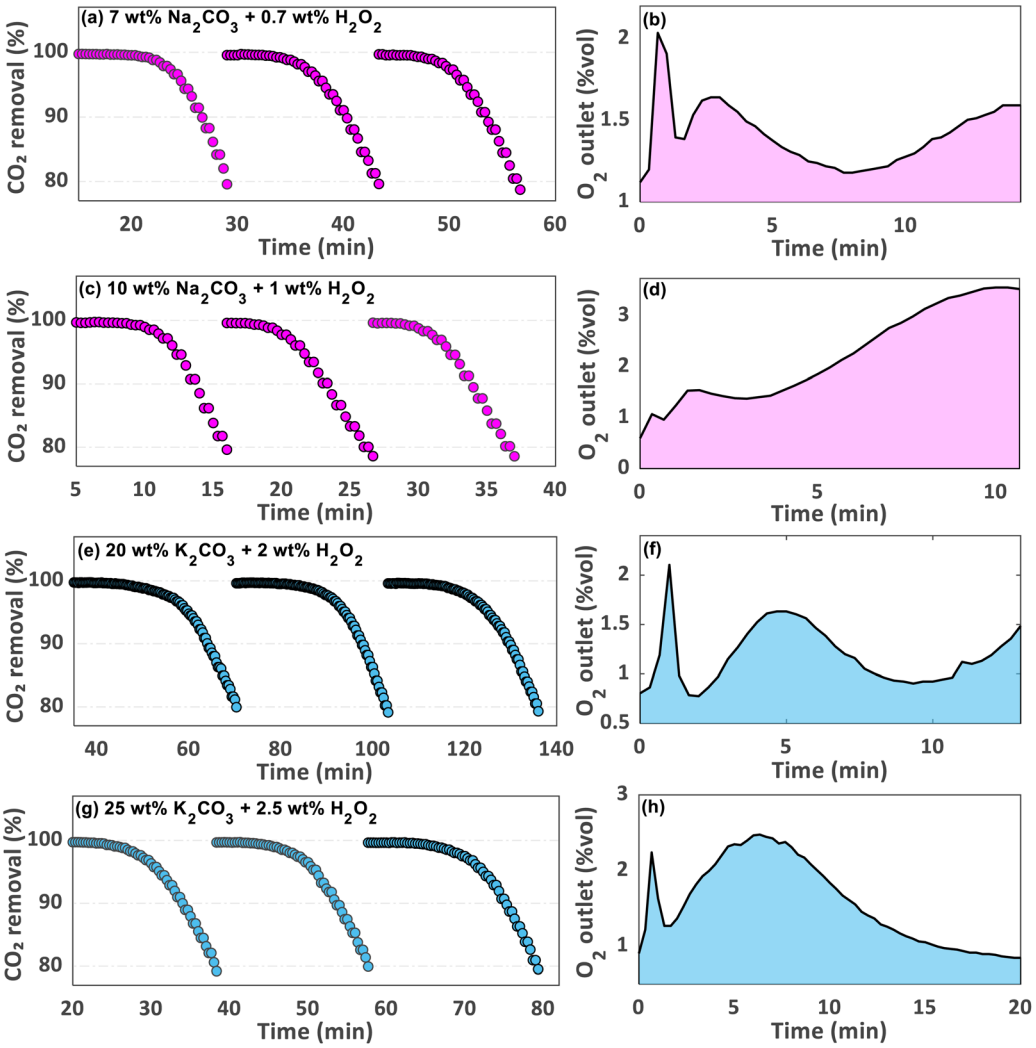

Fig. 5 Cyclic CO_2 absorption in two- and three-reactor trains at 30 °C for four carbonate/H_2O_2 formulations: (a and b) 7 wt% Na_2CO_3 + 0.7 wt% H_2O_2, (c and d) 10 wt% Na_2CO_3 + 1 wt% H_2O_2, (e and f) 20 wt% K_2CO_3 + 2 wt% H_2O_2, and (g and h) 25 wt% K_2CO_3 + 2.5 wt% H_2O_2. Panels (a, c, e and g) show train-averaged CO_2 removal efficiency over three cycles; panels (b, d, f and h) show corresponding O_2 outlet traces for cycle 2. Each cycle was terminated at 80% CO_2 removal. Three-reactor trains (a, b, e and f) operated at 0.5 L min^{-1}; two-reactor trains (c, d, g and h) at 0.35 L min^{-1}.

observed when adding a third stage at those concentrations. Each cycle was terminated when the train-averaged CO_2 removal efficiency reached a set threshold of 80%; the panels display these cut-off runs. After each cycle, the lead reactor was removed for $CaCl_2$ treatment, the train advanced one position, and a fresh solution was loaded at the tail.

In panels (a, c, e and g), each cycle starts with a plateau at complete CO_2 removal, followed by a decline until the 80% threshold is reached. Cycle 1 is longest, whereas cycles 2 and 3 are shorter and nearly equal in duration, as they start with two partially spent stages and only one fresh stage, demonstrating replicability.

The O_2 outlet profiles (panels b, d, f and h) indicate the sequential operation of stages. Each O_2 peak marks the point at which a downstream stage first receives appreciable CO_2 slip while still at high pH (HO_2^--rich). As absorption drives the local pH toward the HO_2^-/H_2O_2 boundary, promoter activity in that stage subsides and its O_2 signal declines until the next stage enters operation. Once the final stage crosses this boundary, residual capacity collapses and the train-averaged removal falls, resulting in the end of the cycle. In (panels b and f), three well-resolved peaks are observed, consistent with three-reactor trains operating at high pH. For two-reactor trains, the 25 wt% K_2CO_3 + 2.5 wt% H_2O_2 case (panel h) similarly exhibits two distinct peaks. By contrast, in the 10 wt% Na_2CO_3 + 1 wt% H_2O_2 case (panel d), the lower sweep flow (0.35 L min^{-1}), together with the greater O_2 peak intensity from Na_2CO_3-treated H_2O_2 (relative to K_2CO_3 at equal mass), causes the two stage contributions to merge into a broad, slightly delayed hump rather than two distinct peaks.

Fig. 6 shows how first-stage conversion in multistage systems changes as a function of efficiency threshold. The bars report the carbonate-to-bicarbonate conversion from ^{13}C NMR measured at the end of cycle 2 for 7 and 10 wt% Na_2CO_3 and 20 and 25 wt%

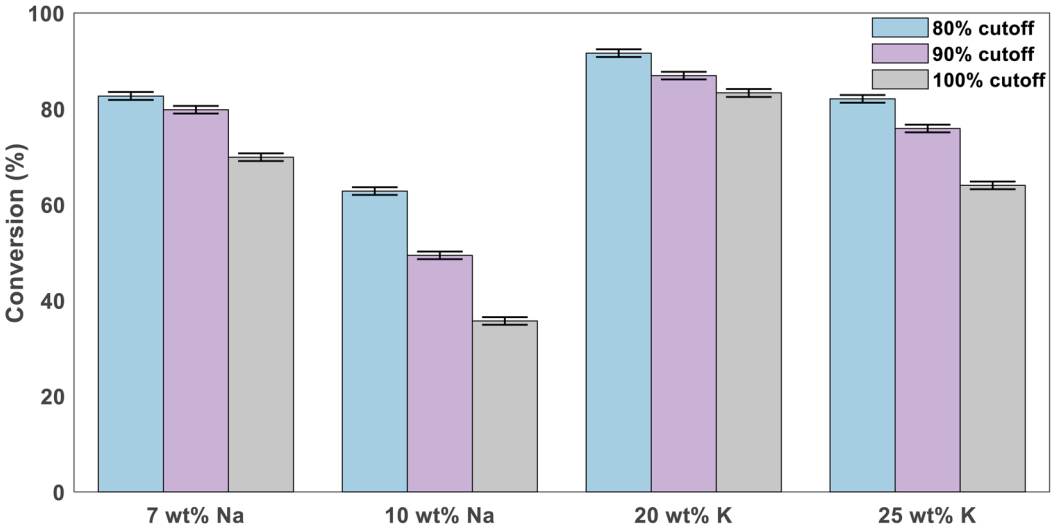

Fig. 6 First-stage carbonate-to-bicarbonate conversion at the end of cycle 2 for 7 and 10 wt% Na_2CO_3 solutions and 20 and 25 wt% K_2CO_3 solutions, each promoted with H_2O_2, as a function of efficiency cutoff (80%, 90%, and 100%).

K_2CO_3, each run at three thresholds: 80% (cyan), 90% (purple), and 100% (grey). Tightening the outlet specification shortens the cycle and therefore reduces conversion, but the magnitude of that penalty depends strongly on formulation. 20 wt% K_2CO_3 remains highly converted across thresholds (about 95% at 80%, ~90% at 90%, ~85% at 100%). 25 wt% K_2CO_3 shows a moderate decline (~80%, ~70%, ~60–65%). 7 wt% Na_2CO_3 stays high at 80 and 90% (about 85–90%) but drops at 100% (~70%). 10 wt% Na_2CO_3 is the most sensitive, falling from about 75–80% at 80% to ~50–55% at 90% and ~35–40% at 100%. These results show that K-based liquors tolerate stricter outlet specifications because they remain homogeneous and promoter-active at higher concentration, whereas Na-based liquors suffer a larger conversion penalty when the threshold is tightened.

The pH evolution of representative reactor-1 liquors at the 90% cutoff supports the proposed self-terminating promotion mechanism (Table 2). The fresh 7 wt% Na_2CO_3 + 0.7 wt% H_2O_2 and 25 wt% K_2CO_3 + 2.5 wt% H_2O_2 liquors start at pH 10.80 and 11.40, respectively, consistent with sufficiently alkaline conditions for peroxide activation. By the cycle-termination point, the pH decreases to 9.00 (cycle 1) and 9.20 (cycle 2) for the Na-based liquor and to 9.47 (cycle 1) and 9.28 (cycle 2) for the K-based liquor. These values are well below the HO_2^-/H_2O_2 acid–base boundary discussed above, consistent with attenuation of the O_2 signal and loss of promoter activity as CO_2 loading proceeds. After $CaCl_2$ addition, the recovered brines show still lower pH values, 8.10 for the Na system and 6.25 for the K system,

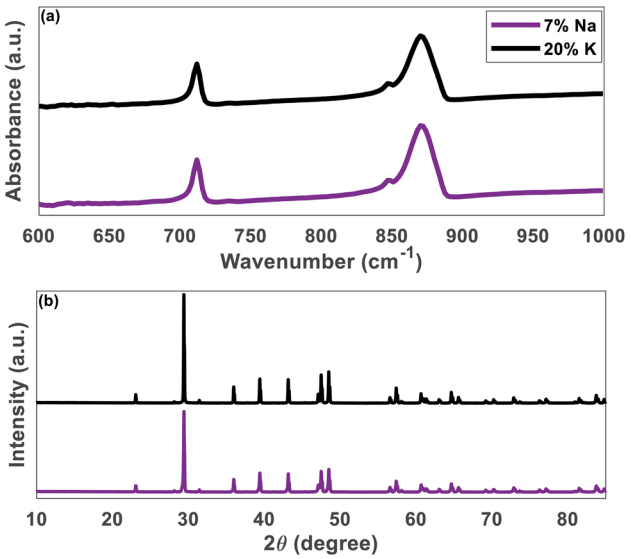

Fig. 7 (a) ATR-FTIR spectra and (b) XRD patterns of $CaCO_3$ precipitates obtained from 7 wt% Na_2CO_3 + 0.7 wt% H_2O_2 and 25 wt% K_2CO_3 + 2.5 wt% H_2O_2 solutions at 30 °C.

confirming that mineralization is carried out on CO_2-loaded liquors that are no longer strongly alkaline. The close agreement between the cycle-1 and cycle-2 cutoff pH values also supports the reproducibility of the stage-swap protocol at the 90% threshold.

Table 2 pH at key process stages for reactor 1 in representative multi-reactor runs operated at the 90% CO_2-removal threshold

Process stage	7 wt% Na_2CO_3 + 0.7 wt% H_2O_2	25 wt% K_2CO_3 + 2.5 wt% H_2O_2
Fresh starting solution before cycle 1	10.80	11.40
End of cycle 1, before $CaCl_2$ addition	9.00	9.47
End of cycle 2, before $CaCl_2$ addition	9.20	9.28
Post-mineralization brine	8.10	6.25

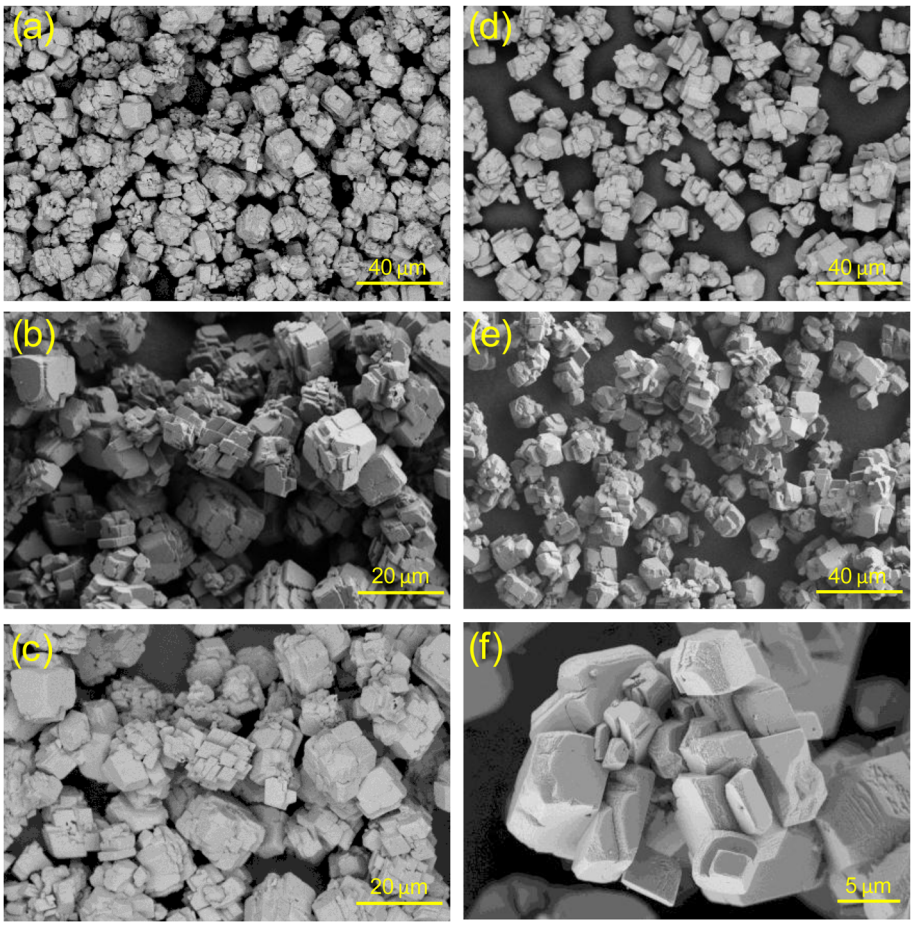

Fig. 8 SEM micrographs of $CaCO_3$ precipitates from (a–c) 7 wt% Na_2CO_3 + 0.7 wt% H_2O_2 and (d–f) 25 wt% K_2CO_3 + 2.5 wt% H_2O_2 solutions at 30 °C.

3.3 Product characterization: $CaCO_3$ phase and morphology

Calcium carbonate was precipitated by adding $CaCl_2$ to the bicarbonate-rich liquors at 30 °C; the temperature was maintained during dosing to prevent cooling-induced precipitation of the absorber prior to conversion.

To quantify the efficiency of the $CaCl_2$-induced precipitation, the isolated $CaCO_3$ yield was determined gravimetrically. After addition of stoichiometric $CaCl_2$ to the post-absorption liquor at 30 °C, the precipitated $CaCO_3$ was collected by filtration, washed with deionized water, and dried at 60 °C to constant mass. The isolated yield was calculated as the ratio of recovered dry $CaCO_3$ mass to the theoretical $CaCO_3$ mass corresponding to the $CaCl_2$ charge (1 mol Ca^{2+} → 1 mol $CaCO_3$). On this basis, the isolated $CaCO_3$ yields were 97.9% for the 7 wt% Na_2CO_3 + 0.7 wt% H_2O_2 case and 98.7% for the 25 wt% K_2CO_3 + 2.5 wt% H_2O_2 case.

Fig. 7 presents ATR-FTIR spectra and XRD patterns of the solids, and Fig. 8 presents SEM micrographs, for the two cases carried through the study: 7 wt% Na_2CO_3 + 0.7 wt% H_2O_2 and 25 wt% K_2CO_3 + 2.5 wt% H_2O_2.

The ATR-FTIR spectra in Fig. 7a are consistent with calcite within the plotted range. Both samples exhibit characteristic bands near 870–875 cm^{-1} and 712–714 cm^{-1}, assigned to the out-of-plane and in-plane bending modes of carbonate, respectively. Bands characteristic of vaterite or aragonite are not evident within the plotted ranges. The XRD patterns are consistent with rhombohedral calcite, showing the expected diffraction peaks and no additional peaks attributable to other $CaCO_3$ polymorphs or crystalline impurities. Within the detection limits of FTIR and XRD, the products from the Na-derived and K-derived liquors are indistinguishable and correspond to phase-pure calcite.

Morphology is consistent with this assignment. The SEM micrographs in Fig. 8 show aggregates of well-faceted rhombohedral crystallites for both liquors. At lower magnification the solids appear as dense, grape-like agglomerates. Higher-magnification views reveal individual crystals bounded by flat faces and stepped edges typical of calcite. Needle-like forms associated with aragonite and spherical cauliflower morphologies associated with vaterite are not observed. Qualitatively, both products comprise micron-scale crystallites with moderate polydispersity; the K-derived material tends to show slightly sharper faceting, while the Na-derived sample appears somewhat more aggregated, yet the dominant habit in both cases remains rhombohedral calcite. Elemental compositions determined by EDS (Tables S1 and S2) further support this assignment, showing only Ca, O, and C, with no detectable secondary

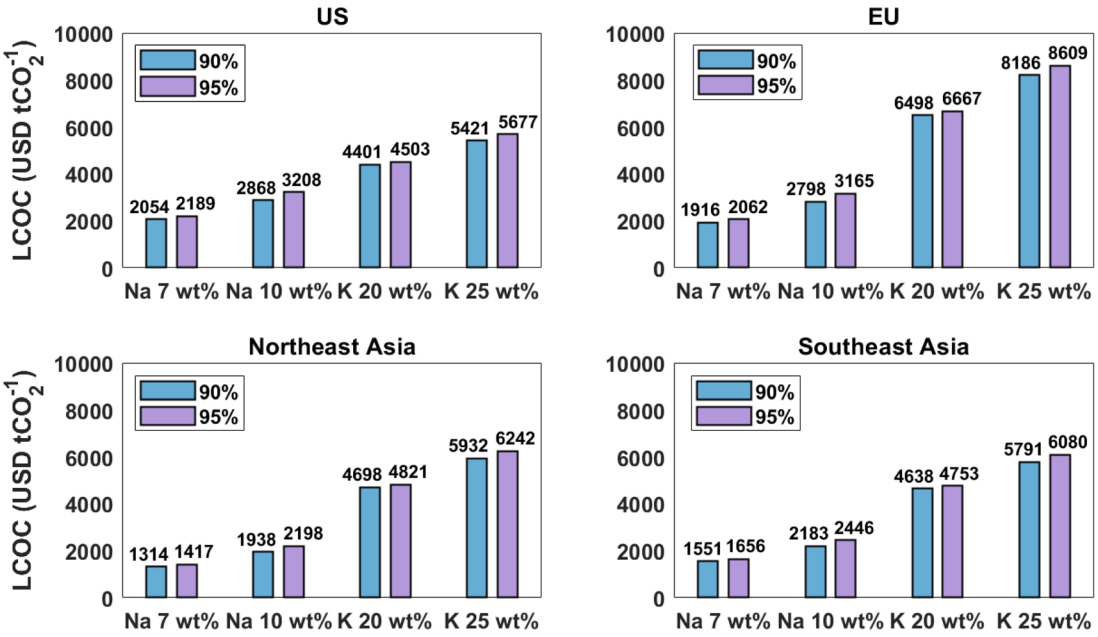

Fig. 9 Consumables-only (upper-bound) levelized cost of capture (LCOC, USD per tCO_2) for representative Na_2CO_3 and K_2CO_3 liquors at 90% and 95% CO_2 removal, evaluated using four geography-specific reagent price decks (US, EU, Northeast Asia, and Southeast Asia; 2025 Q3). Values are derived from measured carbonate utilization at 90% and 100% CO_2 removal and linear interpolation to 95% (Section 3.2); supporting price inputs, utilization factors, and calculation assumptions are provided in the SI (Tables S3 and S4).

elements, consistent with $CaCO_3$. Additional SEM/EDS outputs supporting Fig. 8 and the calcite assignment are provided in the SI (Fig. S1–S6). Representative SEM micrographs for the Na- and K-derived products (Fig. S1 and S4) confirm the same rhombohedral calcite habit observed in Fig. 8. Corresponding EDS spectra (Fig. S2 and S5) show only Ca, C, and O signals, while elemental maps (Fig. S3 and S6) confirm spatially uniform Ca/O/C distributions.

Collectively, ATR-FTIR, XRD, and SEM show that step-2 precipitation at 30 °C yields phase-pure calcite, with no detectable metastable polymorphs, for both Na_2CO_3- and K_2CO_3-derived liquors. This consistency shows that differences in alkali, concentration, and reactor staging during the absorption stage do not lead to mixed-phase $CaCO_3$ during precipitation at 30 °C, simplifying product handling and underscoring the robustness of the capture-to-conversion sequence.

3.4 Techno-economic implications of the multireactor operation

3.4.1 Scope. Fig. 9 reports the consumables-only levelized cost of capture (LCOC; USD per tCO_2), excluding capital and energy contributions, for four geography-specific reagent price decks (US, EU, Northeast Asia, and Southeast Asia; all from 2025 Q3). Because the present scheme is a non-regenerative, capture-to-mineral route, this consumables-only LCOC should be interpreted as a conservative upper bound based on stoichiometric reagent purchase. We report this boundary-transparent metric to isolate how measured carbonate utilization and staging translate into reagent consumption, while allowing absolute LCOC to reflect regional reagent-price differences rather than site-specific CAPEX and energy assumptions or uncertain coproduct and policy values. This approach follows TEA best-practice emphasis on explicit system boundaries and intended use for early stage/screening comparisons.[38] Four representative liquors were considered, Na_2CO_3 (7 and 10 wt%) and K_2CO_3 (20 and 25 wt%), at train-averaged outlet specifications of 90% and 95% CO_2 removal. The 95% values were obtained by linear interpolation between the measured carbonate utilizations at 90% and 100% removal (see Section 3.2). Detailed geography-specific price inputs are provided in Table S3, utilization factors in Table S4, and the underlying calculation assumptions are summarized in the SI.

3.4.2 Definition. The consumables LCOC is defined as:

$$\mathrm{LCOC} = \underbrace{\mathrm{Price}(\mathrm{CaCl_2})\cdot 2.522}_{\mathrm{CaCl_2}} + \underbrace{\mathrm{Price}(\mathrm{carbonate})\cdot \frac{\mathrm{stoich_{carb}}}{u(\mathrm{spec})}}_{\mathrm{carbonate}} + \underbrace{\mathrm{Price}(\mathrm{H_2O_2})\cdot \frac{0.10\cdot \mathrm{stoich_{carb}}}{u(\mathrm{spec})}}_{\mathrm{H_2O_2}}, \quad (5)$$

where u(spec) is the measured carbonate utilization at the selected outlet specification, and the reagent-price terms correspond to the selected geography-specific price deck. The $CaCl_2$ term is fixed at 2.522 t tCO_2^{-1} (1 mol mol^{-1} basis). The carbonate requirements are 2.408 t Na_2CO_3 or 3.140 t K_2CO_3 per tCO_2, each scaled by $1/u$. The H_2O_2 term is modelled as 10 wt% of the carbonate dose (normalized to 100% H_2O_2), and scaling with $1/u$. No coproduct credits are applied for the CO_2 product stream, the $CaCO_3$ product, or brine handling/avoidance; accordingly, the values in Fig. 9 represent a conservative reagent-purchase upper bound rather than a net commercial cost.

3.4.3 Results. Across all four geography-specific price decks, tightening the outlet specification from 90% to 95% increases the consumables-only LCOC for every formulation. This increase directly reflects the reduction in first-stage utilization measured in Section 3.2, whereas the absolute LCOC level varies by geography because the underlying reagent prices differ among the regional decks. Across all four decks, sodium formulations consistently show lower absolute costs owing to their lower stoichiometric mass and lower unit price, whereas potassium formulations are consistently more costly. Notwithstanding this higher absolute cost, the 20 wt% K_2CO_3 case shows a smaller relative penalty upon tightening the outlet specification from 90% to 95%.

Because both the carbonate and promoter terms scale as $1/u$, maintaining high first-stage utilization through reactor staging and appropriate stage-swap timing is the primary lever for controlling consumables cost at tighter outlet specifications. Accordingly, despite variation in absolute LCOC across geography-specific reagent price decks, stoichiometric make-up demand emerges as the dominant cost lever within this consumables-only framework. Future TEAs should therefore prioritize strategies that reduce stoichiometric make-up demand, including (i) improving first-stage utilization at tight specifications, (ii) substituting purchased $CaCl_2$/alkali with low-cost waste brines or by-product alkalinity,[34] and (iii) evaluating reagent regeneration/looping[35,36] and explicit credit scenarios for $CaCO_3$ and brine management.[34]

4 Conclusions

This work demonstrates an ambient-temperature aqueous CO_2 capture-to-conversion route in which ROS-promoted carbonate absorption is coupled to direct chemical precipitation of $CaCO_3$, without heat-driven regeneration. Transient ROS formed *in situ* from H_2O_2-activated alkali carbonates substantially enhance CO_2 uptake at 30 °C, enabling rapid conversion of carbonate to bicarbonate without the need for persistent promoters. The promoter activity diminishes as the alkalinity approaches the HO_2^-/H_2O_2 equilibrium boundary, marking a self-terminating mechanism that leaves a clean bicarbonate solution suitable for downstream mineralization.

Single-reactor screening defined the concentration and time windows that maximize capacity while avoiding premature precipitation, identifying optimal conditions near 7–10 wt% Na_2CO_3 and 20–25 wt% K_2CO_3. Multi-reactor staging was shown to sustain high CO_2-removal efficiencies while preserving carbonate utilization, thereby reducing the trade-off between outlet specification and conversion. K_2CO_3 systems exhibited greater operational stability and higher conversion than their Na-based counterparts, consistent with their higher solubility and broader homogeneous operating window.

Reaction of the bicarbonate-rich liquors with $CaCl_2$ yielded phase-pure rhombohedral calcite, confirmed by XRD, ATR-FTIR, SEM, and EDS analyses, regardless of alkali type or reactor configuration. The process consistently produced dense, well-faceted crystallites with no detectable vaterite or aragonite, underscoring the robustness of the capture-to-conversion sequence.

A consumables-only techno-economic analysis across four geography-specific reagent price decks revealed that the levelized cost of capture (LCOC) is strongly governed by carbonate utilization, with higher first-stage conversion and optimized staging providing the most effective means to minimize cost penalties at tighter CO_2 specifications. The present economics are therefore reagent-dominated, with the main cost-reduction levers being improved carbonate utilization and access to low-cost calcium/alkalinity sources and/or reagent looping. These constitute clear priorities for future scale-up studies, alongside scenario-based inclusion of coproduct and policy crediting. Overall, this study establishes a simple, ambient-temperature pathway that integrates accelerated CO_2 absorption with mineralization, eliminates the need for thermal regeneration, and yields a pure solid carbonate product suitable for utilization or storage.

Conflicts of interest

There are no conflicts to declare.

Data availability

All data supporting the findings of this study are available within the article and its supplementary information (SI). Additional underlying datasets, including raw and processed CO_2/O_2 outlet time-series for single- and multi-reactor experiments, original ^{13}C NMR, XRD and ATR-FTIR files, SEM micrographs and EDS outputs, and the consumables-only LCOC calculation workbook, are available from the corresponding author upon reasonable request. Supplementary information; supporting SEM/EDS characterization of the $CaCO_3$ products, including SEM micrographs, EDS spectra, elemental maps, and elemental analysis tables, as well as supporting information for the consumables-only LCOC analysis, including regional reagent price decks, utilization factors, and calculation assumptions. See DOI: https://doi.org/10.1039/d6su00210b.

References

1 S. J. Davis, N. S. Lewis, M. Shaner, S. Aggarwal, D. Arent, I. L. Azevedo, S. M. Benson, T. Bradley, J. Brouwer, Y. M. Chiang, C. T. M. Clack, A. Cohen, S. Doig, J. Edmonds, P. Fennell, C. B. Field, B. Hannegan,

B. M. Hodge, M. I. Hoffert, E. Ingersoll, P. Jaramillo, K. S. Lackner, K. J. Mach, M. Mastrandrea, J. Ogden, P. F. Peterson, D. L. Sanchez, D. Sperling, J. Stagner, J. E. Trancik, C. J. Yang and K. Caldeira, *Science*, 2018, **360**, eaas9793.

2 M. R. Allen, D. J. Frame, C. Huntingford, C. D. Jones, J. A. Lowe, M. Meinshausen and N. Meinshausen, *Nature*, 2009, **458**, 1163–1166.

3 S. A. Matlin, G. Mehta, S. E. Cornell, A. Krief and H. Hopf, *RSC Sustain.*, 2023, **1**, 1704–1721.

4 M. Bui, C. S. Adjiman, A. Bardow, E. J. Anthony, A. Boston, S. Brown, P. S. Fennell, S. Fuss, A. Galindo, L. A. Hackett, J. P. Hallett, H. J. Herzog, G. Jackson, J. Kemper, S. Krevor, G. C. Maitland, M. Matuszewski, I. S. Metcalfe, C. Petit, G. Puxty, J. Reimer, D. M. Reiner, E. S. Rubin, S. A. Scott, N. Shah, B. Smit, J. P. M. Trusler, P. Webley, J. Wilcox and N. Mac Dowell, *Energy Environ. Sci.*, 2018, **11**, 1062–1176.

5 E. S. Sanz-Pérez, C. R. Murdock, S. A. Didas and C. W. Jones, *Chem. Rev.*, 2016, **116**, 11840–11876.

6 D. Y. C. Leung, G. Caramanna and M. M. Maroto-Valer, *Renew. Sustain. Energy Rev.*, 2014, **39**, 426–443.

7 G. T. Rochelle, *Science*, 2009, **325**, 1652–1654.

8 S. Y. W. Chai, L. H. Ngu and B. S. How, *Greenhouse Gases: Sci. Technol.*, 2022, **12**, 394–427.

9 N. Yi, M. Fang, W. Di, Z. Xia, T. Wang and Q. Wang, *Environ. Sci. Technol.*, 2021, **55**, 5152–5160.

10 K. Veltman, B. Singh and E. G. Hertwich, *Environ. Sci. Technol.*, 2010, **44**, 1496–1502.

11 H. Sun, S. Sun, T. Liu, J. Zeng, Y. Wang, Z. Yan and C. Wu, *ACS Catal.*, 2024, **14**, 15572–15589.

12 C. Hepburn, E. Adlen, J. Beddington, E. A. Carter, S. Fuss, N. Mac Dowell, J. C. Minx, P. Smith and C. K. Williams, *Nature*, 2019, **575**, 87–97.

13 F. Barzagli, C. Giorgi, F. Mani and M. Peruzzini, *J. CO2 Util.*, 2017, **22**, 346–354.

14 G. Hu, N. J. Nicholas, K. H. Smith, K. A. Mumford, S. E. Kentish and G. W. Stevens, *Int. J. Greenhouse Gas Control*, 2016, **53**, 28–40.

15 H. Knuutila, H. F. Svendsen and M. Anttila, *Int. J. Greenhouse Gas Control*, 2009, **3**, 143–151.

16 T. N. G. Borhani, A. Azarpour, V. Akbari, S. R. Wan Alwi and Z. A. Manan, *Int. J. Greenhouse Gas Control*, 2015, **41**, 142–162.

17 H. Thee, K. H. Smith, G. da Silva, S. E. Kentish and G. W. Stevens, *Chem. Eng. J.*, 2012, **181–182**, 694–701.

18 K. Yu, W. A. Mitch and N. Dai, *Environ. Sci. Technol.*, 2017, **51**, 11522–11536.

19 S. Shen, Y. Yang and S. Ren, *Fluid Phase Equilib.*, 2014, **367**, 38–44.

20 J. T. Cullinane and G. T. Rochelle, *Ind. Eng. Chem. Res.*, 2006, **45**, 2531–2545.

21 H. Thee, N. J. Nicholas, K. H. Smith, G. da Silva, S. E. Kentish and G. W. Stevens, *Int. J. Greenhouse Gas Control*, 2014, **20**, 212–222.

22 K. Gustafsson, R. Sadegh-Vaziri, S. Grönkvist, F. Levihn and C. Sundberg, *Int. J. Greenhouse Gas Control*, 2021, **110**, 103434.

23 R. Ramezani and R. Di Felice, *Green Energy Environ.*, 2021, **6**, 83–90.

24 P. Wang, A. Pei, Z. Chen, P. Sun, C. Hu, X. Wang, N. Zheng and G. Chen, *Nat. Commun.*, 2025, **16**, 1–10.

25 X. M. Hu, H. Q. Liang, A. Rosas-Hernández and K. Daasbjerg, *Chem. Soc. Rev.*, 2025, **54**, 1216–1250.

26 E. Shirman and Y. Sasson, *Greenhouse Gases: Sci. Technol.*, 2024, **14**, 1037–1048.

27 J. L. Roberts, M. M. Morrison and D. T. Sawyer, *J. Am. Chem. Soc.*, 1978, **100**, 329–330.

28 L. J. Csyányi, Z. M. Galbács and L. Horváth, *Inorg. Chim. Acta*, 1981, **55**, 1–4.

29 D. E. Richardson, H. Yao, K. M. Frank and D. A. Bennett, *J. Am. Chem. Soc.*, 2000, **122**, 1729–1739.

30 J.-M. Lin and M. Liu, *Spectrochim. Acta, Part A*, 2009, **72**, 126–132.

31 U. Stoin, A. I. Shames, I. Malka, I. Bar and Y. Sasson, *ChemPhysChem*, 2013, **14**, 4158–4164.

32 U. Stoin, Z. Barnea and Y. Sasson, *RSC Adv.*, 2014, **4**, 36544–36552.

33 L. Ji, H. Yu, K. Li, B. Yu, M. Grigore, Q. Yang, X. Wang, Z. Chen, M. Zeng and S. Zhao, *Appl. Energy*, 2018, **225**, 356–366.

34 A. Sanna, M. Uibu, G. Caramanna, R. Kuusik and M. M. Maroto-Valer, *Chem. Soc. Rev.*, 2014, **43**, 8049–8080.

35 Q. Shu, L. Legrand, P. Kuntke, M. Tedesco and H. V. M. Hamelers, *Environ. Sci. Technol.*, 2020, **54**, 8990–8998.

36 D. W. Keith, G. Holmes, D. St. Angelo and K. Heidel, *Joule*, 2018, **2**, 1573–1594.

37 R. Bar and Y. Sasson, *Anal. Chim. Acta*, 1982, **142**, 345–347.

38 A. W. Zimmermann, J. Wunderlich, L. Müller, G. A. Buchner, A. Marxen, S. Michailos and R. Schomäcker, *Front. Energy Res.*, 2020, **8**, 5.